NUCL SCI TECH (2020) 31:98
https://doi.org/10.1007/s41365-020-00813-7

Ion-beam-assisted characterization of quinoline-insoluble particles in nuclear graphite

Qing Huang[1] · Xin-Qing Han[2] · Peng Liu[2] · Jian-Jian Li[1] · Guan-Hong Lei[1] · Cheng Li[1]

Received: 29 June 2020 / Revised: 30 July 2020 / Accepted: 1 August 2020 / Published online: 9 October 2020
© China Science Publishing & Media Ltd. (Science Press), Shanghai Institute of Applied Physics, the Chinese Academy of Sciences, Chinese Nuclear Society and Springer Nature Singapore Pte Ltd. 2020

Abstract The irradiation behavior of graphite is essential for its applications in the nuclear industry. However, the behavioral differences of graphite remain obscure because of the very limited comprehension of its microstructural differences. One typical structure, the quinoline-insoluble (QI) particle, was investigated using IG-110 and NBG-18 graphite. After irradiation, the QI particles on the polished surface were proven to become hillocks, which were easily identifiable via scanning electron microscopy (SEM). Thus, a method that combined ion irradiation and SEM characterization was proposed to study the distribution and concentration of QI particles in graphite. During irradiation, the QI particles were found to evolve into densified spheres, which were weakly bonded with the surrounding graphite structures, thereby indicating that the densification of QI particles did not evidently contribute to graphite dimensional shrinkage. A much higher concentration of QI particles in NBG-18 than IG-110, which was suggested to be responsible for the smaller maximum dimensional shrinkage of former over the latter during irradiation, was characterized.

Keywords Heavy ion irradiation · Nuclear graphite · Quinoline insoluble · Microstructure

1 Introduction

Despite its use in fission reactors for over 70 years, graphite is still proposed to be the neutron moderator and reflector material in two types of Generation IV reactors: molten salt reactors and very high-temperature reactors. The goals of Generation IV reactors are to improve fission reactions in terms of sustainability, safety, and reliability, as well as economics, proliferation resistance, and physical protection. Structural materials for Generation IV reactors usually serve in a high-temperature and intense neutron irradiation environment. The irradiation behavior of a graphite material has to be evaluated to determine its suitability as a neutron moderator or reflector in Generation IV reactors.

Nuclear grade graphite is known to be of high purity, as well as polycrystalline and near-isotropic. Graphite is usually produced from a coke (petroleum coke or pitch coke) and pitch binder. Even though the graphitization temperature for a nuclear graphite product could be as high as 3000 °C, typical structures in the raw materials leave their marks in the final product (such as the filler sizes and the concentration of quinine insoluble (QI) particles). Given the different sources of raw materials and various processing technologies adopted by manufacturers, commercial nuclear graphite grades exhibit very different properties, as well as dissimilar behaviors during neutron irradiation.

Neutron irradiation produces displaced atoms in nuclear graphite, leading to an expansion in the *c*-axis and a

---

This work was supported by Youth Innovation Promotion Association of the Chinese Academy of Sciences (No. 2019262) and the National Natural Science Foundation of China (Nos. 11505265, 11805256, 11805261).

✉ Qing Huang
huangqing2012@sinap.ac.cn

[1] Shanghai Institute of Applied Physics, Chinese Academy of Sciences, Shanghai 201800, China

[2] School of Physics, State Key Laboratory of Crystal Materials, Key Laboratory of Particle Physics and Particle Irradiation (MOE), Shandong University, Jinan 250100, China

shrinkage in graphite basal planes. Countless graphite crystallites in artificial graphite materials evolve and interact with one another and adjacent porosity, thereby resulting in changes in graphite volume, as well as mechanical and thermal properties. Based on previously derived irradiation data from neutron irradiation experiments, the dimensions of nuclear graphite usually have a tendency to initially decrease and increase thereafter [1, 2]. The maximum dimensional shrinkage and the doses whereat the dimensional change reaches the maximum and returns to zero are different for various nuclear graphites.

The historical nuclear grades of graphite are currently unavailable. Therefore, investigations into the irradiation behaviors of commercial graphite grades for their applications in very high-temperature reactors remain ongoing [1, 3]. These irradiation programs include many grades of graphite from different countries, which are intended to reach high doses at various temperatures. Although they are costly and time-consuming, these programs are necessary today and extremely important for the development of next-generation graphite-moderated reactors. For molten salt reactors, the molten salt is in direct contact with the graphite components. To prevent salt penetration, the graphite pores should have sizes smaller than 1 μm, which may be achieved using a ultra-fine-grained coke filler [4, 5]. While the development of suitable graphite for molten salt reactors is still ongoing, the irradiation behavior of graphite developed for molten salt reactors has not been revealed.

It has been reported that the size and cost of a graphite irradiation program “can be significantly reduced through understanding the relationships between the graphite microstructure and properties” [6]. Furthermore, given the need to simulate and predict the behavior of nuclear graphite [7], typical microstructures and their responses to irradiation should be fully understood. There have been many studies on graphite microstructures that are irradiated with neutrons [8–11], electrons [12–14], and ions [15–17]. Irradiation-induced effects on the atomic level, including the decreasing sp^2 content, fragmentation, and distortion of graphite basal planes, decreasing *a*-lattice parameter, increasing *c*-lattice parameter, dislocation dipole, and climb of dislocations in the graphite lattice, were reported. It was suggested that irradiation-induced effects in graphite may be considered to have two components: “bulk microstructural effects” and “intrinsic lattice effects” [8]. The “intrinsic lattice effects” described above are apparently common in all graphite materials. However, the “bulk microstructural effects” lead to the divergent behaviors of nuclear graphite during irradiation. However, the microstructural difference between various graphite grades has not been well studied. Karthik et al. [18] investigated the microstructures of three types of graphite (NBG-18, IG-110, and PCEA) via transmission electron microscopy (TEM) and expressed that NBG-18 contains a higher concentration of QI and chaotic structures than the other two.

The QI particle, once referred to as rosettes, is a typical nuclear graphite structure. Notably, QI particles have a near-spherical appearance and contain many packets of graphite sheets that are arranged concentrically [19]. Moreover, TEM has usually been adopted to characterize the QI particles in nuclear graphite [8, 18]. Although the concentration of QI particles was reported to vary, their influence on the irradiation behaviors of nuclear graphite remains unrevealed. In this study, two nuclear graphite grades were irradiated with energetic xenon ions at high temperature. The evolution of QI particles during irradiation was observed and explained, which provides a new way to determine the distribution and concentration of QI particles in graphite. After irradiation to a high dose, the structures, including QI particles, were characterized. The influence of QI particles on volume changes in graphite during irradiation is also discussed.

2 Materials and methods

2.1 Materials

Two types of graphite were used in this study. The IG-110 graphite, from Toyo Tanso Inc., is produced from petroleum coke with an average grain size of ∼ 20 μm. TheNBG-18 graphite, from SGL Group, is manufactured from pitch coke with a maximum grain size of 1600 μm. According to the standard ASTM D7219, NBG-18 and IG-110 are regarded as medium-grained and superfine-grained graphite, respectively. Typical properties of the two graphite grades are listed in Table 1.

Firstly, samples of the two graphite grades were ground using a 1500-grit emery paper to remove the entire original rough surface. Thereafter, the samples were polished successively on a cloth using 3000-nm and 50-nm diamond suspensions. Notably, mechanical polishing produces surface defects, thereby resulting in an increase in the D peak intensity in the Raman spectrum. However, a flat surface is obtainable through polishing and is suitable for analyzing the evolutions of filler particles, pores, and other microstructures during irradiation. The polished samples were cut into small slices (length × width × thickness: $7 \times 1.5 \times 1$ mm^3) for irradiation.

2.2 Ion irradiation

Two samples, IG-110 and NBG-18, were irradiated by $(7 + 4 + 2)$ million electron volt (MeV) xenon ions.

Table 1 Typical properties of IG-110 and NBG-18 graphite

	Density (g/cm^3)	Compressive strength (MPa)	Tensile strength (MPa)	Flexural strength (MPa)	Coefficient of thermal expansion (10^{-6}/K)	Thermal conductivity (W/m/K)	Young's modulus (GPa)
IG-110	1.77	78	25	39	4.5	120	9.8
NBG-18	1.85	80	20	30	4.5	140	11.5

Irradiation was performed at the 320 kV high-voltage Experimental Platform in the Institute of Modern Physics, Chinese Academy of Science. Twenty-six electrons were stripped off the xenon atoms (Xe^{26+}) to attain the energy of 7 meV, while twenty electrons were stripped off (Xe^{20+}) to reach the energy of 2 and 4 meV. Xenon ions are adopted in this study because they are chemically inert and can create displaced carbon atoms at high speeds. Multi-energy xenon ions were chosen to irradiate the samples in this study to produce a uniformly damaged layer in samples. The xenon ion beam was scanned in two directions. An annular Faraday cup was used as an aperture in front of the target for uniform irradiation by the xenon ions. The sample was fixed on a metallic plate facing the xenon ion beam. The metallic plate was installed in the middle of a circular heater, and the temperature of the sample was maintained to 600 °C during irradiation. The temperature of the sample was measured and monitored by a thermocouple. Another Faraday cup was placed behind the target to measure the ion beam passing through the aperture. When the target is mounted and ready for irradiation, the ion beam is blocked by the target and cannot be measured by the Faraday cup. Therefore, the current of the ion beam was monitored during irradiation by the annular Faraday cup in front of the target. The beam currents of the xenon ions were recorded to be in the range of 1.6–2.6 μA. A high vacuum (pressure $< 5 \times 10^{-4}$ Pa) in the irradiation chamber was kept during heating and irradiation.

The xenon ion irradiation process was simulated using "The Stopping and Range of Ions in Matter" (SRIM) program. A displacement threshold energy (E_d) value is required for a proper SRIM simulation. Upon evaluating the neutron irradiation-induced displacements in carbon materials, the value of E_d was reported to be 31 eV [20]. A theoretical study reported that the E_d had a value of 25 eV at 300 K [21]. At a temperature of 900 K, the value of E_d increases to 30 eV [21], which is approximately the value used to calculate the neutron irradiation damage. Therefore, a value of 31 eV was applied for E_d in this study. Notably, changing the value of E_d only alters the calculated number of displacement atoms and does not influence their profile.

Subsequently, SRIM simulations with two modes—"Ion Distribution and Quick Calculation of Damage" and "Detailed Calculation with full Damage Cascades"—were performed to calculate the number of displacement atoms. The number of displacements in nickel and iron calculated using these two modes was compared with that derived from the well-known model developed by Norgett, Robinson, and Torrens (NRT model) [22]. It was found that the SRIM simulation with the "Quick Calculation mode" produced displaced atoms in nickel and iron comparable to the NRT model, while the "full Damage Cascade mode" produced much more displaced atoms [23]. Therefore, the SRIM calculation with the "Quick Calculation mode" has been recommended. However, in the case of xenon ion irradiation into graphite, the number of displaced atoms calculated with the SRIM program with the two modes is comparable and is 1/3 less than those derived from the NRT model. In this study, inert xenon ion irradiation at high temperatures was applied to graphite to simulate the neutron irradiation damage, which had been calculated using the NRT model [20]. Therefore, a number of displaced atoms derived from the NRT model were used and were determined to be 19,180, 14,916, and 10,026 displacements/ion for 7, 4, and 2 meV xenon ions, respectively. Next, the profile of displacements per atom (dpa) was derived from the ion fluence (ions/cm^2). The dose was accumulated to 4, 15, and 25 dpa, where 1 dpa is equal to $(8.6 + 3.44 + 2.58) \times 10^{14}$ ions/cm^2.

2.3 Characterization techniques

Thin foils of un-irradiated graphite were prepared for TEM observation. Samples with diameters of ~ 3 mm were cut from the un-irradiated graphite materials and were then ground to disks with thicknesses of ~ 50 μm. A dimple grinder was used to further grind the center of the disks. Thereafter, a penetration hole was formed in the disks by low-energy (3–5 keV) argon ion milling using a Gatan Model 691 system. A 200 kV FEI Tecnai G2 F20 TEM was used to characterize the QI particles in the two graphite grades. In addition, the NBG-18 sample was heated to 600 °C during TEM observation for in situ electron irradiation. The electron beam (200 kV), with a diameter of ∼ 100 nm and current of ∼ 15 nA, was focused on one QI particle. The image of the QI particle was captured every 2 min during irradiation. The electron fluences were accumulated to 1.4×10^{23}, 2.8×10^{23}, 4.2×10^{23}, and 5.6×10^{23} electrons/cm^2.

One specimen for TEM characterization was also prepared for the NBG-18 graphite sample irradiated to 25 dpa to investigate the structures of the irradiated QI particles. To observe the cross section of the irradiated sample, two slices were cut from the xenon-ion-irradiated NBG-18 sample. The irradiated surfaces of the two slices were glued facially. The edges of the specimen were milled until they could be inserted into a 3-mm-diameter copper tube. Then, the tube was cut into small pieces. The remaining processing steps with the small pieces are the same as those mentioned above.

The surface of the polished samples was observed via scanning electron microscopy (SEM) before and after ion irradiation to 15 and 25 dpa to study the surface morphology changes and QI particle evolution during irradiation.

The Raman scattering spectra were collected from the NBG-18 graphite before irradiation and after irradiation at each dose. A Bruker SENTERRA confocal Raman microscope was used to measure the Raman spectra at room temperature. The excitation beam has a wavelength of 532 nm.

A simple fit with two symmetric Lorentzians is often used for the Raman spectra of crystalline graphite structures. Nevertheless, two-peak fitting is unsuitable for the Raman spectra of highly disordered carbon materials. Typically, a fit with four symmetric peaks (D peak, G peak, and two other peaks) involving Gaussian lines has been used for the Raman spectra of highly disordered carbon materials. However, four Gaussian lines can usually provide good fitting with more than one possibility for the Raman spectra of highly disordered graphite. A unique and appropriate four-peak fit cannot be distinguished from all the possibilities, which may cause an inconsistency in interpreting the Raman spectra of irradiated graphite within various studies.

Rather than using a four-peak fitting, the Raman spectra were fitted with a symmetric Lorentzian for the D peak and an asymmetric Breit–Wigner–Fano (BWF) line for the G peak in this study [24]. Because of the peak broadening induced by irradiation, the small D′ peak that emerged in the Raman spectrum of the as-polished graphite was unrecognizable after xenon ion irradiation. Therefore, the fitting of the D′ peak was not conducted.

3 Results

3.1 The QI particles in graphite before irradiation

Figure 1 shows a typical QI particle in IG-110 graphite. There are many small packets of graphite sheets in QI particles. Empty voids were found in-between the packets. The *c*-axis of these packets is directed radially toward the center of the QI particles [19]. Usually, QI particles are surrounded by folded graphite structures, which are shown outside the dashed circle in Fig. 1.

TEM micrographs of QI particles in NBG-18 andIG-110 graphite are shown in Fig. 2a, b, respectively. It is evident that QI particles tend to agglomerate in nuclear graphite. The concentration of QI particles in IG-110 is much less than that in NBG-18 graphite, which is consistent with the conclusion of the previous study [18].

3.2 Identifying the QI particles on irradiated graphite surface

The SEM micrographs of the irradiated surfaces of NBG-18 and IG-110 are shown in Fig. 3a, b, respectively. The polished surface became rough after irradiation. Wrinkle-like textures (marked by W) are found on the surfaces of both graphite samples. These wrinkle-like textures were first identified on needlelike fillers in the IG-110 graphite after argon ion irradiation [15]. Therefore, they are believed to be the graphite structures with the long-range order. The “wrinkles” show the directions of curved graphite sheets. The size of the wrinkle-like textures represents the size of these graphite structures.

The main difference between the surface morphology of the two types of graphite is the concentration of small

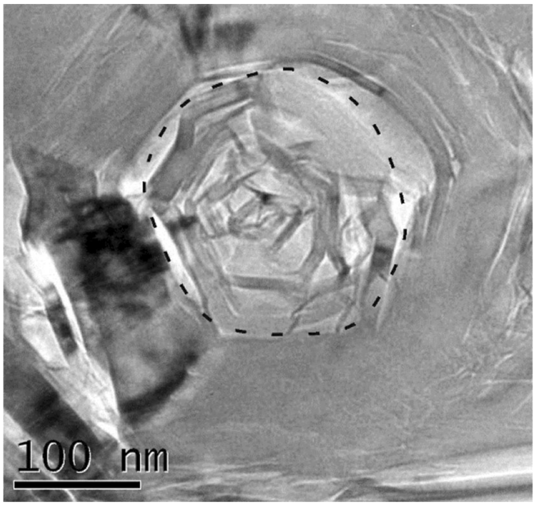

Fig. 1 TEM micrograph of a typical QI particle (indicated by a dashed circle)

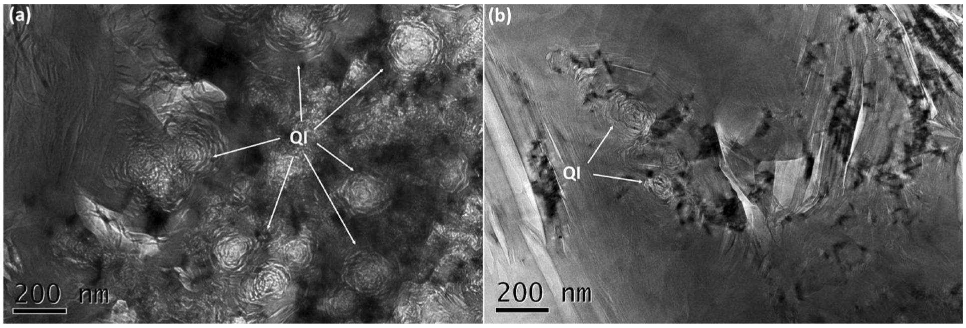

Fig. 2 TEM micrographs of microstructures with QI particles in **a** NBG-18 and **b** IG-110

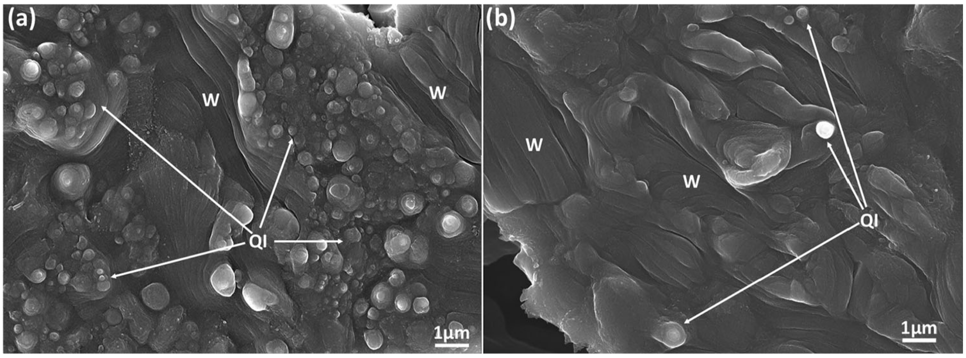

Fig. 3 SEM micrographs of polished surfaces of **a** NBG-18 and **b** IG-110 after irradiation to 15 dpa. The "wrinkle-like" structures shown on the irradiated surface are marked by "W."

round hillocks (indicated by arrows in Fig. 3). These hillocks have very small sizes and tend to agglomerate, especially in NBG-18. Therefore, they are considered to be the QI particles. To prove this ideology, two QI particles were identified on the as-polished surface of the NBG-18 sample (Fig. 4a). Typical QI particle features, loose cores surrounded by folded graphite sheets (indicated by two dashed circles), are evident in Fig. 4a. After irradiation, two hillocks emerged at the same place. Apparently, the hillocks, especially the left-hand side one, shrink radially and grow in height during irradiation. Faint round wrinkles are found on the two hillocks.

To show the distribution of QI particles in NBG-18 graphite, Fig. 5 shows an SEM micrograph of the irradiated NBG-18 surface. The entire irradiated surface is occupied by agglomerations of hillocks, along with the wrinkle-like structures. Large cracks, shown in Fig. 5, which are formed during the calcination of the filler coke, are typical for the fillers of NBG-18 graphite. This kind of calcination cracks is also present in the fillers of nuclear graphite Gilsocarbon and PCEA [19, 25]. Figure 5 reveals an area in a typical filler of NBG-18 graphite. It was interesting to see a large number of QI particles in the filler since they were always reported to be formed in the binder phase [8, 19]. Based on the morphology of the irradiated NBG-18 surface, it can be deduced that the filler in NBG-18 graphite is composed of many graphite structures (represented by the wrinkle-like structures with sizes from several microns to tens of microns), which are separated by the agglomerations of QI particles (represented by the hillocks).

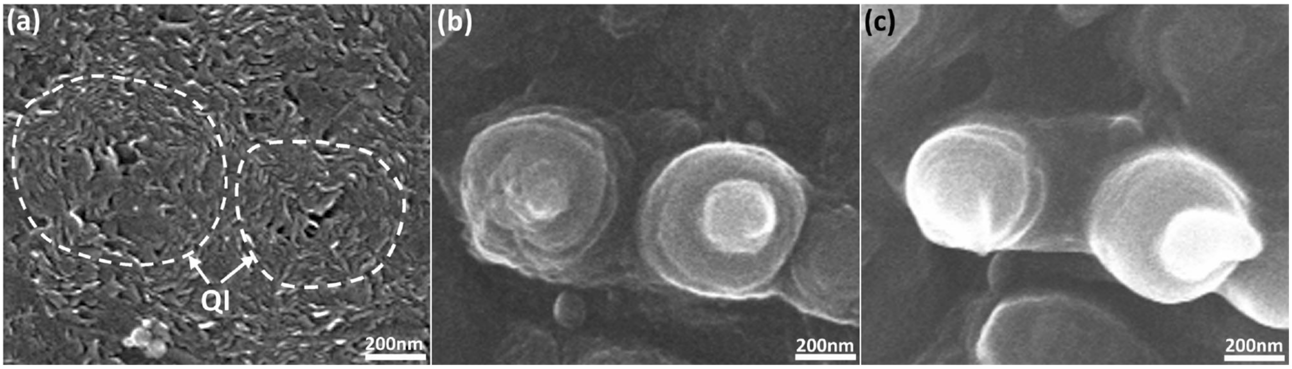

Fig. 4 SEM micrographs showing two QI particles evolve into hillocks. **a** Two QI particles indicated by dashed circles on the as-polished surface, **b** after irradiation at 15 dpa, and **c** after irradiation at 25 dpa

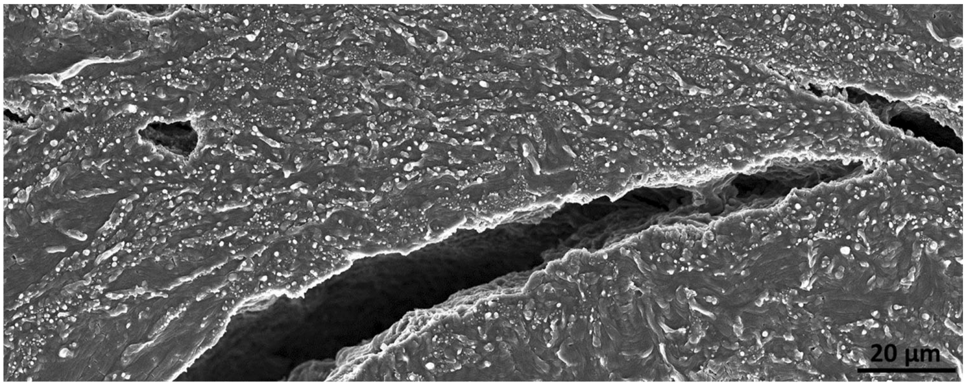

Fig. 5 SEM micrograph of irradiated NBG-18 surface showing calcination cracks and a large number of hillocks

3.3 The Raman spectra of irradiated graphite

The Raman spectra were measured at the regions of QI particle agglomeration on the polished NBG-18 surface. Figure 6a shows the Raman spectra before and after xenon ion irradiation. The irradiation doses are also shown in Fig. 6a. Three peaks (the G mode appearing at 1582 cm^{-1}, the D mode located at $\sim$ 1350 cm^{-1}, and the small peak D′ at 1620 cm^{-1}) emerged in the spectrum of un-irradiated graphite. During xenon ion irradiation, the graphite structures were damaged gradually by nuclear collisions, resulting in peak broadening and overlapping.

Figure 6b, c shows the full width at half maximum (FWHM) of the G peak and the ratio of the intensities of D and G peaks (I_D/I_G), respectively. The FWHM of the G mode of the as-polished NBG-18 sample is $\sim$ 30 cm^{-1}. During xenon ion irradiation at 600 °C, the FWHM increased monotonically to a value of $\sim$ 150 cm^{-1}(25 -dpa). It was reported that the irradiation-induced disordering of the graphite lattice might cause a strong coupling between the discrete G mode and a continuum of phonon states, resulting in the broadening of the G peak [26].

The D mode was explained as a "breathing mode" of sp^2 carbon atom rings and was forbidden in a perfect graphite lattice [10]. In-plane defects have to be introduced into graphite to excite the D peak. The region of agglomeration of QI particles contains many small graphitic structures with abundant defects in boundaries. Therefore, the I_D/I_G ratio was high (0.84), even without irradiation. At the beginning of irradiation, although the number of in-plane defects increased, a sufficient amount of carbon atom rings was preserved, resulting in an increase in the D peak intensity with limited overlapping of peaks [27]. It has been reported that the I_D/I_G ratio increases fast and reaches

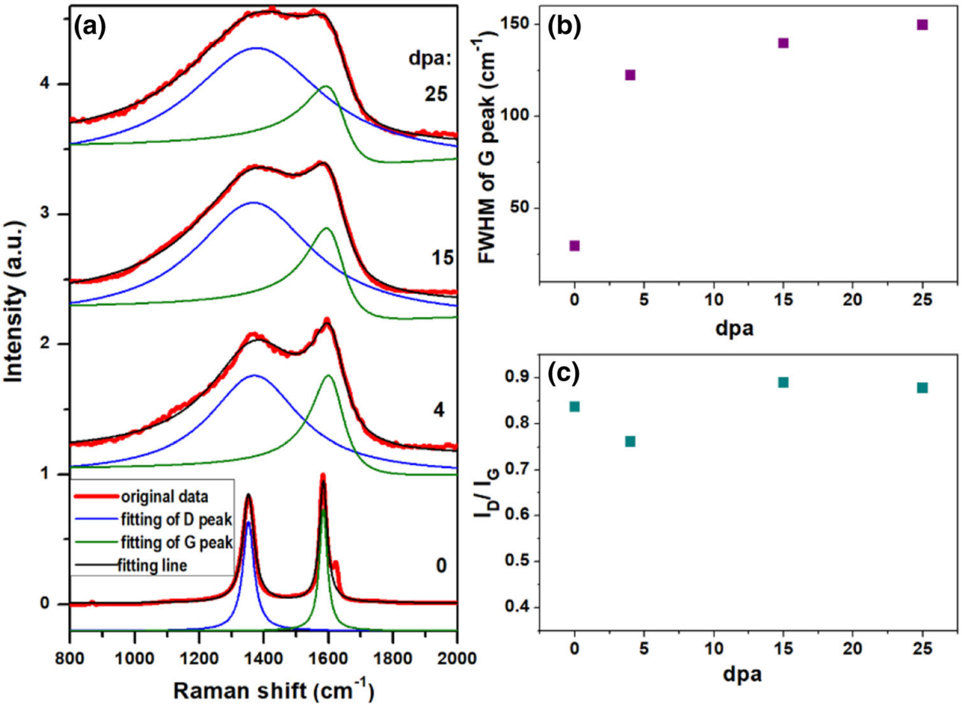

Fig. 6 (Color figure online) **a** The Raman spectra and fitting curves of the agglomeration of QI particles before and after xenon ion irradiation to three doses. **b** The full width at half maximum (FWHM) of the G peak at various doses. **c** I_D/I_G at various doses

a maximum of ~ 1.4 at quite low doses (< 0.02 dpa) for graphite irradiated at room temperature [10, 16, 27]. Along with the increase in the I_D/I_G ratio, the graphite structure evolved into nano-crystalline graphite. With further irradiation, the lattice disordering increased, while the number of ordered rings decreased, resulting in a reduction in the D peak intensity and broadening of Raman scattering peaks. Figure 6a shows that the Raman peaks at 4 dpa are already highly broadened; thus, the maximum of the I_D/I_G ratio should appear at lower doses than 4 dpa. It is worth mentioning that an inversely proportional relationship between the I_D/I_G ratio and the in-plane crystallite size was proposed and has been used to characterize the crystallinity of graphitic structures [28]. However, this relationship can only be used to calculate the crystallite size in the increasing stage of I_D/I_G ratio [24]. At higher irradiation doses, the I_D/I_G ratio decreases, and this relationship is apparently invalid presently.

Both the G peak width and the I_D/I_G ratio tended to be stable at doses higher than 15 dpa, indicating that the graphite structure at high irradiation doses, although damaged, was very stable. It was reported that the I_D/I_G ratio decreased toward 0.2 in an amorphous carbon material [24, 29]. Figure 6c shows that the values of I_D/I_G ratio at high doses are approximately 0.9, indicating that graphite is not amorphous after xenon ion irradiation to 25 dpa at 600 °C.

3.4 Irradiation effects in QIs in nuclear graphite

A QI particle was in situ irradiated by the electron beam in TEM at 600 °C. Figure 7a–c shows the QI particle before and after irradiation for 4 and 8 min (with electron fluences of 2.8×10^{23} and 5.6×10^{23} electrons/cm^2), respectively. During irradiation, the small packets of graphite sheets swelled in the *c*-axis and shrank in the basal plane. The *c*-axis swelling was readily absorbed by the voids, and the shrinkage in basal plane resulted in the densification of the QI particle. The black arrows show the evidence of shrinkage of the QI particle. Densification of QI particles has also been reported in neutron-irradiated NBG-18 [8].

Figure 8a shows the TEM micrograph of NBG-18 irradiated to 25 dpa. This TEM sample was processed not only by the xenon ion irradiation but also by subsequent low-energy argon ion milling during the TEM sample preparation. Caution must be exercised to distinguish the damage induced by xenon ion irradiation from that induced by low-energy argon ion milling. Figure 8a shows a highly damaged surface layer with a thickness of ~ 3.1 μm which is consistent with the xenon ion range (3 μm) obtained from the SRIM simulation. Therefore, the damaged surface layer is induced by xenon ion irradiation. The boundary (indicated by a white dashed line) between the xenon-ion-irradiated layer and the un-irradiated substrate was evident in the TEM micrograph. The structures in the substrate were not irradiated by xenon ions but subjected to low-energy argon ion milling. Typical QI particles and graphite structures were found in the un-irradiated substrate, indicating that the damage induced by low-energy argon ion milling could be ignored compared to the damage induced by high-dose xenon ion irradiation.

Many densified QI particles with a spherical appearance are shown in the irradiated layer. Two areas indicated by the dashed squares are magnified in Fig. 8b, c. Irradiated and un-irradiated QI particles are identified in Fig. 8b. The loose core of the QI particles and the surrounding folded graphite sheets shrank and evolved into the densified spheres, which were found to be weakly bonded with the adjacent structures.

There are plenty of lenticular cracks with widths of several nanometers or tens of nanometers shown in Fig. 8a–c. Lenticular cracks are typical structures in nuclear graphite and are known as Mrozowski cracks.

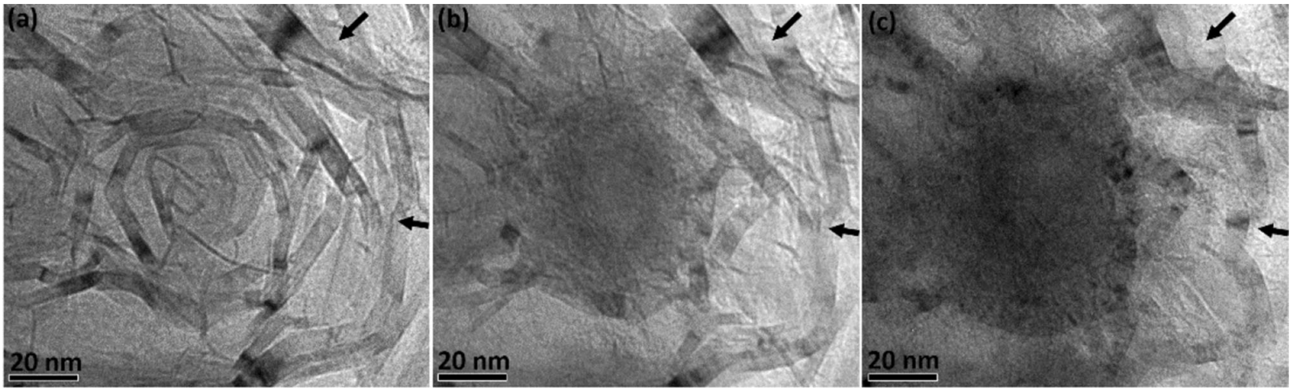

Fig. 7 Evolution of a QI particle in NBG-18 during in situ electron beam irradiation at 600 °C. Electron dose: **a** 0, **b** 2.8×10^{23}, and **c** 5.6×10^{23} electrons/cm^2

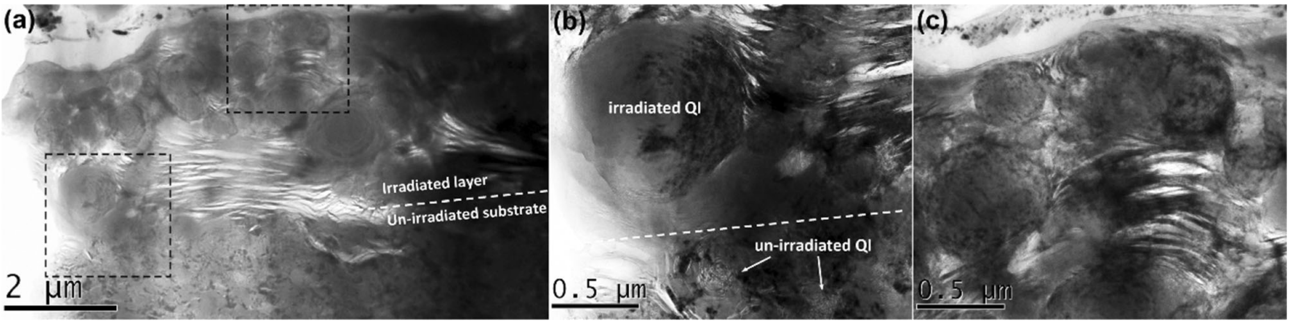

Fig. 8 **a** TEM micrograph of the NBG-18 sample irradiated to 25 dpa. The white dashed line indicates the end of the ion range. The areas indicated by the two black dashed squares are magnified in **b** and **c**

During cooling down from the graphitization temperature, cracks opened between graphite basal planes by anisotropic thermal shrinkage. Both heating and irradiation could cause a remarkable expansion of the graphite structure in the *c*-axis, which could be readily absorbed by these cracks. Owing to these lenticular cracks, graphite has a good resistance to thermal shock and irradiation-induced swelling and disintegration. After irradiation to 25 dpa, graphite structures were expected to swell in the *c*-axis and close the lenticular cracks. However, Fig. 8 reveals that the graphite structures between the QI particles still show plenty of cracks lying between the graphite sheets because of the shrinkage of the adjacent QI particles.

4 Discussion

Since the “hillock” structures were formed on the irradiated surface, they were easily regarded to be the results of sputtering under xenon ion bombardments. The SRIM simulations using the “Monolayer Collision Steps/Surface Sputtering” mode were conducted. The sputtering yield of xenon ions (normal incidence) with energy values of 2, 4, and 7 meV was obtained from SRIM simulation and was 1.63, 1.35, and 0.92 atoms/ion, respectively. In total, irradiation to 25 dpa sputtered 4.19×10^{16} atoms/cm^2, corresponding to only a 4.6-nm-thick graphite layer being stripped off. Therefore, the “hillock” structures that appear on the irradiated graphite surface cannot be produced by sputtering under xenon ion bombardments.

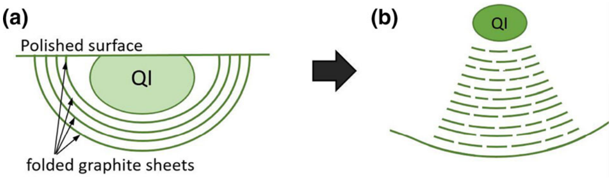

Fig. 9 (Color figure online) Mechanism of hillock formation on the irradiated surface. **a** A QI particle on the polished surface before irradiation, **b** the QI particle after irradiation

An explanation of the emergence of hillocks is shown in Fig. 9. Figure 9a shows a sketch of a QI particle at the polished surface. Therefore, the surrounding graphite sheets are cut on the polished surface. During irradiation, along with the shrinkage of the QI particle, the fractured graphite sheets shrink in basal plane and swell along the *c*-axis. At the beginning of irradiation, the *c*-axis swelling is accommodated by microcracks. The folded graphite sheets surrounding the QI particles (Fig. 1) have very narrow (< ~ 20 nm) and short (< ~ 100 nm) microcracks which can be readily closed by fast *c*-axis swelling. After the microcracks closed, the structure grew along the *c*-axis. Meanwhile, the folded graphite sheets shown in Fig. 9a shrink in the basal plane, resulting in a hillock contracting radially and growing in height during irradiation. Experimental and theoretical studies [14, 30] describe the irradiation-induced fragmentation of graphite sheets, which is also indicated by the segmented lines shown in Fig. 9b.

Notably, TEM has been used to characterize QI particles in nuclear graphite. This is believed to be the first report of SEM characterization of a single QI particle and distributions of QI particles in nuclear graphite. For TEM observation, the field of view is limited to several μm^2 when observing the QI particles in graphite. Conversely, the hillocks can be easily identified via SEM at magnifications of approximately 400 × with the field of view much larger than 10,000 μm^2, which shows the global distribution of QI particles in one graphite. When comparing the concentration of the QI particles between different types of graphite, the SEM characterization of the hillocks is believed to be more convincing than the very local TEM characterization. Furthermore, the SEM micrographs of irradiated graphite evidently show that NBG-18 contains a large number of QI particles with a concentration much higher than that in IG-110.

Eventually, the influence of the QI particles in the volume changes of graphite during neutron irradiation is discussed. However, instead of neutron irradiation, ion irradiation was adopted to study the evolution of the QI particles (Fig. 8). Both ion beam and electron beam irradiation have long been applied rather than the time-consuming and expensive neutron irradiation in studying the irradiation effect in microstructures of structural materials. For highly pure nuclear graphite, the changes in the mechanical and thermal properties induced by neutron irradiation are outcomes of atom displacement damage, which can also be produced much faster by ion irradiation. Energetic neutrons and ions have different tracks in graphite. Neutrons barely interact with electrons and lose their energy through nuclear collision, leading to a very deep track in the target. Ions interact with both electrons and nuclei and only leave a very short track in the target. The neutrons could create primary knocked-on atom (PKA) in the entire sample (centimeter size), while the ions only create PKAs on the surface of the sample (micron size). However, after being produced by ions or neutrons, PKAs are ions and create the most part of displaced atoms in the target. Therefore, similar effects are expected for both ion and neutron irradiation. Actually, the well-known neutron irradiation effects, such as irradiation-induced dislocations, *d*-spacing increase, lenticular crack closing, shrinkage in basal plane, and swelling in the *c*-axis, have been reported in ion irradiated graphite [15, 31]. Creep of graphite induced by proton irradiation was reported to simulate the in-reactor creep of graphite [32]. Nano-indentation tests performed on nuclear graphite samples irradiated by carbon ions or protons show an increase in modulus, which is consistent with the neutron irradiation effects in graphite [27, 33]. Therefore, the ion beams are suitable for studying irradiation effects in graphite microstructures. Notably, swift heavy ions should be avoided when simulating neutron irradiation effects in nuclear graphite. Very high electron excitation could be produced by swift heavy ions, leaving a disordered ion track in the graphite lattice [34]. The energy of the ion transferred to target electrons has to surpass a threshold value to form an observable ion track. A threshold value of 730 eV/angstrom has been reported for graphite [34]. By SRIM simulation, the peak value of electron excitation caused by 7 meV xenon ions is 250 eV/angstrom, which is smaller than the threshold value. Disordered ion tracks could not be formed by electronic energy deposition in this study. Xenon ions used herein are believed to create defects in graphite only by nuclear collisions, in the same way as during neutron irradiation.

All the microstructures (such as long-range ordered graphite structure, microcracks, QI particles, and others) could affect the bulk property changes during irradiation. Although the NBG-18 was manufactured with fillers much larger than those used for IG-110, this study shows that the long-range ordered graphite structures (indicated by “wrinkles” shown on irradiated surface) within the two graphite grades have similar sizes. On the submicron scale, we did not discover apparent differences in microcracks between the two graphite grades via TEM. The most remarkable difference between the two graphite grades is the concentration of QI particles. Although QI particles are densified after irradiation, the bonding between the densified QI particles and the adjacent graphite structures is weak and the lenticular cracks within the adjacent graphite structures are not effectively closed (Fig. 8). The QI particles should shrink independently during irradiation. Therefore, it is believed that the densification of the QI particles does not evidently contribute to the shrinkage of graphite during irradiation.

The volume changes of NBG-18 and IG-110 during neutron irradiation at 750 °C have been recently revealed [1]. Given the scattering of the irradiation data, the maximum dimensional shrinkage of the NBG-18 graphite and IG-110 graphite can be estimated to be $-$ 4.5% and $-$ 5%, respectively. The NBG-18 graphite shows a smaller maximum volume shrinkage than IG-110 graphite, which is suggested to be because of the much higher concentration of QI particles in NBG-18 graphite.

5 Conclusion

One typical microstructure of nuclear graphite, the QI particle, was investigated in this study. The QI particles were found to evolve into hillocks on the irradiated surface of graphite, making ion irradiation combined with SEM characterization an effective technique to study their distribution and concentration in various nuclear grades of graphite. The shrinkage of a QI particle was directly observed during in situ electron irradiation via TEM. Furthermore, the TEM characterization of xenon-ion-irradiated NBG-18 graphite shows that the QI particles evolved into densified spheres, which are weakly bonded with the surrounding graphite structures. It is believed that the densification of QI particles does not evidently contribute to graphite volume shrinkage during irradiation. High-temperature xenon ion irradiation induced a continuous increase in the Raman G peak width of graphite. However, at doses $>$ 15 dpa, both the G peak width and I_D/I_G ratio tended to be stable, indicating a stable graphitic structure (although damaged) in nuclear graphite. The concentration of QI particles in NBG-18 is characterized to be much higher than that in IG-110, which is suggested to be why NBG-18 has a smaller maximum dimensional shrinkage than IG-110 during irradiation.

References

1. M.C.R. Heijna, S. de Groot, J.A. Vreeling, Comparison of irradiation behaviour of HTR graphite grades. J. Nucl. Mater. **492**, 148–156 (2017). https://doi.org/10.1016/j.jnucmat.2017.05.012
2. S. Ishiyama, T.D. Burchell, J.P. Strizak et al., The effect of high fluence neutron irradiation on the properties of a fine-grained isotropic nuclear graphite. J. Nucl. Mater. **230**, 1–7 (1996). https://doi.org/10.1016/0022-3115(96)00005-0
3. S.B. Grover, Status of the NGNP graphite creep experiments AGC-1 and AGC-2 irradiated in the advanced test reactor. Nucl. Eng. Des. **271**, 275–282 (2014). https://doi.org/10.1016/j.nucengdes.2013.11.048
4. J. Wang, S. Feng, Y. Yang et al., Microstructure evolution of IG-110 nuclear graphite with salt infiltration revealed by in-situ tensile synchrotron-XRD. Nucl. Tech. **42**, 040106 (2019). https://doi.org/10.11889/j.0253-3219.2019.hjs.42.040106. **(in Chinese)**
5. H. Tang, Z. He, C. Zhang et al., Equipment design and experiment of compatibility test of nuclear graphite and molten salt. Nucl. Tech. **41**, 070605 (2018). https://doi.org/10.11889/j.0253-3219.2018.hjs.41.070605. **(in Chinese)**
6. B.J. Marsden, M. Haverty, W. Bodel et al., Dimensional change, irradiation creep and thermal/mechanical property changes in nuclear graphite. Int. Mater. Rev. **61**, 155–182 (2016). https://doi.org/10.1080/09506608.2015.1136460
7. X. Yang, Y.-T. Gao, Y. Zhong et al., Stress analysis of the TMSR graphite component under irradiation conditions. Nucl. Sci. Tech. **29**, 173 (2018). https://doi.org/10.1007/s41365-018-0516-8
8. C. Karthik, J. Kane, D.P. Butt et al., Neutron irradiation induced microstructural changes in NBG-18 and IG-110 nuclear graphites. Carbon **86**, 124–131 (2015). https://doi.org/10.1016/j.carbon.2015.01.036
9. H.M. Freeman, B.E. Mironov, W. Windes et al., Micro to nanostructural observations in neutron irradiated nuclear graphites PCEA and PCIB. J. Nucl. Mater. **491**, 221–231 (2017). https://doi.org/10.1016/j.jnucmat.2017.05.011
10. J. Eapen, R. Krishna, T.D. Burchell et al., Early damage mechanisms in nuclear grade graphite under irradiation. Mater. Res. Lett. **2**, 43–50 (2014). https://doi.org/10.1080/21663831.2013.841782
11. R. Krishna, J. Wade, A.N. Jones et al., An understanding of lattice strain, defects and disorder in nuclear graphite. Carbon **124**, 314–333 (2017). https://doi.org/10.1016/j.carbon.2017.08.070
12. J. Koike, D.F. Pedraza, Dimensional changes in highly oriented pyrolytic graphite due to electron-irradiation. J. Mater. Res. **9**, 1899–1907 (1994). https://doi.org/10.1557/jmr.1994.1899
13. C. Karthik, J. Kane, D.P. Butt et al., In situ transmission electron microscopy of electron-beam induced damage process in nuclear grade graphite. J. Nucl. Mater. **412**, 321–326 (2011). https://doi.org/10.1016/j.jnucmat.2011.03.024
14. B.E. Mironov, H.M. Freeman, A.P. Brown et al., Electron irradiation of nuclear graphite studied by transmission electron microscopy and electron energy loss spectroscopy. Carbon **83**, 106–117 (2015). https://doi.org/10.1016/j.carbon.2014.11.019
15. Q. Huang, H. Tang, Y. Liu et al., Pore structure evolution of IG-110 graphite during argon ion irradiation at 600°C. J. Mater. Sci. **54**, 6098–6110 (2019). https://doi.org/10.1007/s10853-019-03329-7
16. K. Niwase, T. Tanabe, Defect structure and amorphization of graphite irradiated by D^+ and He^+. Mater. Trans. JIM **34**, 1111–1121 (1993). https://doi.org/10.2320/matertrans1989.34.1111
17. W. Qi, Z.T. He, B.L. Zhang et al., Behaviors of fine (IG-110) and ultra-fine (HPG-510) graphite irradiated by 7 MeV $Xe26^+$ ions. Nucl. Sci. Tech. **28**, 144 (2017). https://doi.org/10.1007/s41365-017-0292-x
18. C. Karthik, J. Kane, D.P. Butt et al., Microstructural characterization of next generation nuclear graphites. Microsc. Microanal. **18**, 272–278 (2012). https://doi.org/10.1017/S1431927611012360
19. K.Y. Wen, T.J. Marrow, B.J. Marsden, The microstructure of nuclear graphite binders. Carbon **46**, 62–71 (2008). https://doi.org/10.1016/j.carbon.2007.10.025
20. R. MacFarlane, A.C. Kahler, Methods for processing ENDF/B-VII with NJOY. Nucl. Data Sheets **111**, 2739–2890 (2010). https://doi.org/10.1016/j.nds.2010.11.001
21. A.J. McKenna, T. Trevethan, C.D. Latham et al., Threshold displacement energy and damage function in graphite from molecular dynamics. Carbon **99**, 71–78 (2016). https://doi.org/10.1016/j.carbon.2015.11.040
22. M.J. Norgett, M.T. Robinson, I.M. Torrens, A proposed method of calculating displacement dose rates. Nucl. Eng. Des. **33**, 50–54 (1975). https://doi.org/10.1016/0029-5493(75)90035-7
23. R.E. Stoller, M.B. Toloczko, G.S. Was et al., On the use of SRIM for computing radiation damage exposure. Nucl. Instrum. Methods B **310**, 75–80 (2013). https://doi.org/10.1016/j.nimb.2013.05.008
24. A.C. Ferrari, J. Robertson, Interpretation of Raman spectra of disordered and amorphous carbon. Phys. Rev. B **61**, 14095–14107 (2000). https://doi.org/10.1103/physrevb.61.14095
25. J. Kane, C. Karthik, D.P. Butt et al., Microstructural characterization and pore structure analysis of nuclear graphite. J. Nucl. Mater. **415**, 189–197 (2011). https://doi.org/10.1016/j.jnucmat.2011.05.053
26. B.S. Elman, M.S. Dresselhaus, G. Dresselhaus et al., Raman scattering from ion-irradiated graphite. Phys. Rev. B **24**, 1027–1034 (1981). https://doi.org/10.1103/physrevb.24.1027
27. Q. Huang, Q. Lei, Q. Deng et al., Raman spectra and modulus measurement on the cross section of proton-irradiated graphite. Nucl. Instrum. Methods B **412**, 221–226 (2017). https://doi.org/10.1016/j.nimb.2017.09.004
28. F. Tuinstra, J.L. Koenig, Raman spectrum of graphite. J. Chem. Phys. **53**, 1126–1130 (1970). https://doi.org/10.1063/1.1674108
29. D.G. McCulloch, S. Prawer, A. Hoffman, Structural investigation of xenon-ion-beam-irradiated glassy carbon. Phys. Rev. B **50**, 5905–5917 (1994). https://doi.org/10.1103/PhysRevB.50.5905
30. A. Chartier, L. Van Brutzel, J. Pageot, Irradiation damage in nuclear graphite at the atomic scale. Carbon **133**, 224–231 (2018). https://doi.org/10.1016/j.carbon.2018.03.024
31. Q. Huang, Q. Lei, H. Tang et al., Fracture resistance of imperfect filler particles within nuclear graphite during irradiation. Nucl. Instrum. Methods B **464**, 123–127 (2020). https://doi.org/10.1016/j.nimb.2019.12.022
32. A.A. Campbell, G.S. Was, Proton irradiation-induced creep of ultra-fine grain graphite. Carbon **77**, 993–1010 (2014). https://doi.org/10.1016/j.carbon.2014.06.016
33. S.H. Chi, G.C. Kim, Comparison of 3 MeV C^+ ion irradiation effects between the nuclear graphites made of pitch and petroleum cokes. J. Nucl. Mater. **381**, 98–105 (2008). https://doi.org/10.1016/j.jnucmat.2008.08.001
34. J. Liu, R. Neumann, G. Trautmann et al., Tracks of swift heavy ions in graphite studied by scanning tunneling microscopy. Phys. Rev. B **64**, 184115 (2001). https://doi.org/10.1103/PhysRevB.64.184115